

# Solar-cycle Variability of Composite Geometry in the Solar Wind Turbulence

Zhan Fa<sup>1,2</sup> and H.-Q. He<sup>1,2</sup>

Received \_\_\_\_\_; accepted \_\_\_\_\_

---

<sup>1</sup>Key Laboratory of Planetary Science and Frontier Technology, Institute of Geology and Geophysics, Chinese Academy of Sciences, Beijing 100029, China; hqhe@mail.iggcas.ac.cn

<sup>2</sup>College of Earth and Planetary Sciences, University of Chinese Academy of Sciences, Beijing 100049, China

## ABSTRACT

The composite geometry and spectral anisotropy of the solar wind turbulence are very important topics in the investigations of solar wind. In this work, we use the magnetic field and plasma data from Wind spacecraft measured during 1995 January to 2023 December, which covers more than two solar cycles, to systematically investigate these subjects in the context of solar-cycle variability. The so-called spectrum ratio test and spectrum anisotropy test are employed to determine the three-dimensional (3D) geometry of the solar wind turbulence. Both the tests reveal that the solar wind turbulence is dominated by the two-dimensional (2D) component ( $\sim 80\%$  by turbulence energy). More interestingly, we find that the fraction of slab turbulence increases with the rising sunspot number, and the correlation coefficient between the slab fraction and the sunspot number is 0.61 (ratio test result) or 0.65 (anisotropy test result). This phenomenon suggests that the increasing solar activity (signified by sunspot number) causes increasing slab component in the solar wind turbulence. The relationship between spectral anisotropy and solar activity is discussed and explained. The enhancement of slab fraction is associated with the intensified interplanetary magnetic field magnitude and the increased Alfvén speed during the rise phases of the solar cycles. Our findings will be very helpful for achieving a better understanding of the 3D composite geometry and spectral anisotropy of the solar wind turbulence, and especially of their solar-cycle variability.

*Subject headings:* Solar wind (1534); Interplanetary turbulence (830); Magnetohydrodynamics (1964); Space plasmas (1544); Solar cycle (1487); Sunspots (1653)

## 1. Introduction

Interplanetary space, filled with magnetized plasmas, can serve as a unique laboratory for investigating diverse space plasma phenomena. As the primary stellar wind directly detectable, the solar wind provides us an invaluable opportunity to study magnetohydrodynamics (MHD) turbulence (Tu & Marsch 1995; Bruno & Carbone 2013). The solar wind turbulence is related to several crucial topics regarding the physical processes in the interplanetary space, such as energy transfer, momentum exchange, and dynamics of energetic particles (Jokipii & Hollweg 1970; Goldstein et al. 1995; Velli 2003; He 2015, 2021). Recently, the anisotropy of solar wind turbulence has been intensely investigated in the community of space physics and solar physics.

A prominent feature of solar wind turbulence is its anisotropy, which arises from the presence of a mean magnetic field that introduces a preferred direction within the plasmas (Horbury et al. 2008; Wicks et al. 2010). The anisotropy is related to the spatial distribution of turbulent fluctuations and their spectral properties. As a pivotal aspect of solar wind turbulence, spectral anisotropy has drawn considerable attention. The spectral anisotropy is crucial as it governs the cascade of energy from large to small scales and affects the dynamics of wave-particle interactions (Goldreich & Sridhar 1995; Chen 2016). There are three primary models for describing the geometry of solar wind turbulence: the slab model, the two-dimensional (2D) model, and the slab/2D two-component composite model. The so-called slab model posits that the fluctuations propagate strictly parallel to the mean magnetic field (Parker 1979; Zhou & Matthaeus 1990). The 2D model assumes that wavevectors are oriented perpendicular to the mean field, capturing the predominant transverse properties of observed fluctuations (Shebalin et al. 1983; Oughton et al. 1994). However, empirical observations have consistently demonstrated that neither the slab model nor the 2D model alone sufficiently captures the complexity of solar wind turbulence

(Matthaeus et al. 1990; Bieber et al. 1996).

Matthaeus et al. (1990) identified significant discrepancies between theoretical predictions based on pure slab turbulence and observations of cosmic-ray propagation. These discrepancies necessitate incorporating 2D component to reconcile the theoretical models with observational results. Consequently, the two-component composite models combining slab and 2D components were proposed and subsequently supported by observational investigations (Bieber et al. 1996; Dasso et al. 2005). Further insights into the composite property of solar wind turbulence were provided by Matthaeus et al. (1995), who recognized the combined influences of slab and 2D components. Bieber et al. (1996) analyzed the data from Helios 1 and Helios 2 spacecraft, and suggested that the solar wind turbulence for a frequency band in the inertial range is 2D-component dominated ( $\sim 84\%$  of the total turbulence energy). Oughton et al. (2015) and Oughton & Engelbrecht (2021) also reported that the 2D component is predominant in the inertial range, with energy fraction ranging from 50% to 100%.

Utilizing axisymmetric models, Bieber et al. (1996) established two methods, i.e., spectrum ratio test and spectrum anisotropy test, to infer the relative significance of 2D component in the solar wind turbulence during 29 solar proton events. The spectrum ratio test, based on the ratio of perpendicular to parallel spectra, suggested a composite structure with 26% slab component and 74% 2D component for inertial range in solar wind turbulence. The spectrum anisotropy test evaluated the dependence of spectra on the angle between the mean magnetic field and the solar wind velocity. As the angle increases, the parallel spectrum component decreases, while the perpendicular component increases. The anisotropy test suggested a composite structure with 5% slab component and 95% 2D component. Similar results were obtained by Zank & Matthaeus (1992) in Mach number scaling experiments in the frame of incompressible theory. They found that

approximately 80% of turbulence energy is distributed in the 2D component and 20% in the slab component.

The anisotropy of solar wind turbulence is influenced by solar wind conditions. Dasso et al. (2005) found that the parallel turbulence component is significant in fast solar winds, while the quasi-perpendicular (2D) turbulence component is prominent in slow solar winds. Narita (2018) reviewed the wavevector distribution of turbulence energy in different directions, and implied that spectral anisotropy may be influenced by the instability of the mean magnetic fields and plasmas. Osman & Horbury (2007) obtained spatial autocorrelation functions using two-point measurements of magnetic fields from Cluster spacecraft, and gave the value  $1.79 \pm 0.36$  of the ratio of correlation scales along the mean field direction to those along the field-perpendicular directions. Recently, Zhou et al. (2020) investigated the solar-cycle variability of correlation scale, Taylor scale, and effective magnetic Reynolds number in the solar wind turbulence. They found that the correlation coefficient between the Taylor scale and the sunspot number is 0.92, and the correlation coefficient between the effective magnetic Reynolds number and the sunspot number is -0.82. Zhou & He (2021) explored the solar-cycle variability of the anisotropy of solar wind turbulence. Their results revealed that the correlation coefficient between the anisotropy ratios of the Taylor scales and the sunspot number is 0.65, and the correlation coefficient between the anisotropy ratios of the effective magnetic Reynolds number and the sunspot number is -0.75.

In this work, we use the data measured by Wind spacecraft during the long time period 1995 January to 2023 December to investigate the long-term (solar-cycle) variability of the composite geometry and spectral anisotropy of the solar wind turbulence. This paper is arranged as follows. In Section 2, we provide a brief description of the theoretical bases for the two analysis methods of observational data, i.e., the so-called spectrum ratio test

and spectrum anisotropy test. Section 3 describes the data selection criteria, processing techniques, and utilization of the spectral analysis methods. The results are presented and discussed in Section 4, where we examine the influence of solar activity on solar wind turbulence anisotropy. A summary of our findings will be provided in Section 5.

## 2. Models for Anisotropic Spectra

We employ a single-spacecraft technique to determine the 3D anisotropic geometry of solar wind turbulence. This method has been used in a series of works (e.g., Bieber et al. 1996; Horbury et al. 2008; Forman et al. 2011). We establish a right-handed orthogonal coordinate system for investigating the axisymmetric turbulence concerning the local mean magnetic field  $\mathbf{B}_0$ : the  $z$ -axis is aligned with  $\mathbf{B}_0$ , the  $x$ -axis is set to be coplanar with both  $\mathbf{B}_0$  and the solar wind flow velocity  $\mathbf{V}$ , and the  $y$ -axis completes the right-handed orthogonal coordinate frame. The angle  $\psi$  denotes the acute angle between  $\mathbf{B}_0$  and  $\mathbf{V}$ .

For spatially homogeneous turbulence, the power spectral density tensor  $P_{ij}(\mathbf{k})$  can be expressed using the two-point correlation tensor  $R_{ij}(\mathbf{r})$  as

$$P_{ij}(\mathbf{k}) = \frac{1}{(2\pi)^3} \int R_{ij}(\mathbf{r}) e^{-i\mathbf{k}\cdot\mathbf{r}} d^3\mathbf{r}. \quad (1)$$

Here,  $\mathbf{k}$  and  $\mathbf{r}$  denote the wavevector and the spatial separation vector, respectively.

Within the plasma framework, the spacecraft velocities are significantly lower than the solar wind speeds  $V$ , and hence, the Taylor hypothesis (Taylor 1938) is usually applied to relate the local spatial and temporal correlation tensors. Using the material derivative  $D/Dt = \partial/\partial t + V \cdot \nabla$ , we can obtain the relation

$$R_{ij}^{(t)}(\tau) = R_{ij}^{(x)}(-V \sin \psi \tau, 0, -V \cos \psi \tau). \quad (2)$$

Here,  $R_{ij}^{(t)}(\tau)$  is the temporal correlation tensor at time lag  $\tau$ , and  $R_{ij}^{(x)}(\mathbf{r})$  is the spatial correlation tensor.

Considering the magnetic fluctuations  $\mathbf{b} = \mathbf{B} - \mathbf{B}_0$  with  $\langle \mathbf{b} \rangle = 0$ , where  $\langle \cdot \rangle$  denotes an ensemble average, we can obtain the frequency power spectra from the time series measurements of magnetic fluctuations using the following transform expression

$$P_{ij}(f) = \int_{-\infty}^{\infty} R_{ij}^{(t)}(\tau) e^{-i2\pi f\tau} d\tau. \quad (3)$$

Substituting Equation (2) into Equation (3) and using the Fourier transform, we can obtain

$$P_{ij}(f) = \int P_{ij}(\mathbf{k}) \delta \left( f - \frac{\mathbf{k} \cdot \mathbf{V}}{2\pi} \right) d^3\mathbf{k}, \quad (4)$$

where the delta function  $\delta$  can enforce the Doppler shift condition between spatial and temporal frequencies. The feasibility of this transform is rooted in the harmonic analysis of time series, where each stationary time series can be depicted as a summation of Fourier components (Nieuwstadt et al. 2016).

In the domain of wavevectors, the anisotropy is evident in the structures of the energy spectrum, which encompass both parallel and perpendicular components regarding the mean magnetic field (Narita 2018). Slab turbulence is characterized by wavevectors exclusively aligned in the  $\mathbf{B}_0$  direction, while 2D turbulence is defined by wavevectors oriented purely orthogonal to  $\mathbf{B}_0$ . According to the approach suggested by Matthaeus & Smith (1981), the general spectral tensors can be divided into two modes, i.e., the so-called slab model ( $k_x = k_y = 0$ ) and 2D model ( $k_{\parallel} = k_z = 0$ ).

The slab model can be described as

$$\begin{aligned} P_{xx}^S(\mathbf{k}) &= P_{yy}^S(\mathbf{k}) = G_S(k_z) \delta(k_x) \delta(k_y), \\ P_{zz}^S(\mathbf{k}) &= 0. \end{aligned} \quad (5)$$

The 2D model can be expressed as

$$\begin{aligned} P_{xx}^{2D}(\mathbf{k}) &= \frac{G_{2D}(k_{\perp})}{k_{\perp}^3} k_y^2 \delta(k_z), \\ P_{yy}^{2D}(\mathbf{k}) &= \frac{G_{2D}(k_{\perp})}{k_{\perp}^3} k_x^2 \delta(k_z), \\ P_{zz}^{2D}(\mathbf{k}) &= 0, \end{aligned} \quad (6)$$

where  $k_{\perp} = \sqrt{k_x^2 + k_y^2}$ ,  $G_S$  is a function of  $k_z$ ,  $G_{2D}$  is a function of  $k_{\perp}$ , and  $\delta$  denotes the Dirac delta function. Substituting Equations (5) and (6) into Equation (4), we can shift the focus from the wavevector domain to the frequency domain as demonstrated by Bieber et al. (1996) and Zank et al. (2020). The shifted slab model can be written as

$$\begin{aligned} P_{xx}^S(f) = P_{yy}^S(f) &= \frac{2\pi}{V \cos \psi} G_S(k_z), \\ k_z &= \frac{2\pi f}{V \cos \psi}. \end{aligned} \quad (7)$$

The shifted 2D model can be described as

$$\begin{aligned} P_{xx}^{2D}(f) &= \frac{4\pi}{V \sin \psi} \int_{|k_x|}^{\infty} \frac{G_{2D}(k_{\perp})}{k_{\perp}^2} \sqrt{k_{\perp}^2 - k_x^2} dk_{\perp}, \\ P_{yy}^{2D}(f) &= \frac{4\pi}{V \sin \psi} k_x^2 \int_{|k_x|}^{\infty} \frac{G_{2D}(k_{\perp})}{k_{\perp}^2} \frac{1}{\sqrt{k_{\perp}^2 - k_x^2}} dk_{\perp}, \\ k_x &= \frac{2\pi f}{V \sin \psi}. \end{aligned} \quad (8)$$

Differentiating the Equation (8) with respect to the frequency  $f$ , we can clarify the relationship between perpendicular and parallel spectral components in the 2D model as

$$P_{\perp}^{2D}(f) = -f \frac{dP_{\parallel}^{2D}(f)}{df}. \quad (9)$$

In our coordinate system, the  $y$ -axis is orthogonal to the mean magnetic field  $\mathbf{B}_0$ , which is aligned with the  $z$ -axis. For the velocity vectors that lie within the  $x$ - $z$  plane, we can project them onto the direction of the magnetic field. We designate  $P_{yy}(f)$  and  $P_{xx}(f)$  as the perpendicular spectrum  $P_{\perp}(f)$  and the parallel spectrum  $P_{\parallel}(f)$ , respectively. These components can serve as the principal diagonal elements of the spectral tensor. Since  $P_{zz}(f) = 0$  for both models, the total power spectrum can be simplified as

$$P_{\text{total}}(f) = P^S(f) + P^{2D}(f) = P_{\parallel}(f) + P_{\perp}(f). \quad (10)$$

It is usually assumed that  $G_S$  in Equation (7) and the integral term containing  $G_{2D}$  in Equation (8) conform to the power-law distributions (e.g., Bieber et al. 1996; Horbury et al.



2008; Forman et al. 2011; Zank et al. 2020). Specifically, we assume  $G_S(k_z) = A_S k_z^{-q}$ , where  $A_S$  is the amplitude of slab turbulence, and  $q$  is the spectral index. Then from Equation (7) we can infer the following relation

$$fP_{\perp}^S(f) = fP_{\parallel}^S(f) = A_S k_z^{1-q} = A_S \left( \frac{2\pi f}{V \cos \psi} \right)^{1-q}. \quad (11)$$

For the 2D turbulence, we assume  $G_{2D}(k_{\perp}) = A_{2D} k_{\perp}^{-q}$ , where  $A_{2D}$  is the amplitude of 2D turbulence. Evaluating the integrals in Equation (8) and using Equation (9), we can obtain

$$\begin{aligned} fP_{\parallel}^{2D}(f) &= A_{2D} \frac{2}{1+q} \left( \frac{2\pi f}{V \sin \psi} \right)^{1-q}, \\ fP_{\perp}^{2D}(f) &= A_{2D} \frac{2q}{1+q} \left( \frac{2\pi f}{V \sin \psi} \right)^{1-q}. \end{aligned} \quad (12)$$

For anisotropic solar wind turbulence based on the slab+2D composite model, the individual spectra can be written as

$$fP_{\perp}(f) = A_S \left( \frac{2\pi f}{V \cos \psi} \right)^{1-q} + A_{2D} \frac{2q}{1+q} \left( \frac{2\pi f}{V \sin \psi} \right)^{1-q}, \quad (13)$$

and

$$fP_{\parallel}(f) = A_S \left( \frac{2\pi f}{V \cos \psi} \right)^{1-q} + A_{2D} \frac{2}{1+q} \left( \frac{2\pi f}{V \sin \psi} \right)^{1-q}. \quad (14)$$

Dividing Equation (13) by Equation (14) yields

$$\frac{P_{\perp}(f)}{P_{\parallel}(f)} = \frac{r(\cos \psi)^{q-1} + (1-r) \frac{2q}{1+q} (\sin \psi)^{q-1}}{r(\cos \psi)^{q-1} + (1-r) \frac{2}{1+q} (\sin \psi)^{q-1}}, \quad (15)$$

where  $r$  denotes the slab fraction representing the energy in slab mode relative to the total energy (Bieber et al. 1996; Saur & Bieber 1999), i.e.,

$$r = \frac{A_S}{A_S + A_{2D}}. \quad (16)$$

Combining Equations (13) and (14), we can obtain the total power spectrum as

$$fP_{\text{total}}(f) = 2A_S \left( \frac{2\pi f}{V \cos \psi} \right)^{1-q} + 2A_{2D} \left( \frac{2\pi f}{V \sin \psi} \right)^{1-q}. \quad (17)$$

On the right of Equation (17), the first and second terms represent the contributions from slab and 2D modes, respectively. To examine the total energy spectrum at a specific reference frequency  $f_K$ , we reformulate the above equation as

$$f_K P_{\text{total}}(f_K) = E \left[ r(\cos \psi)^{q-1} + (1-r)(\sin \psi)^{q-1} \right], \quad (18)$$

where  $E = 2(A_S + A_{2D})k_{\text{ref}}^{1-q}$  denotes the total amplitude at the reference wavenumber  $k_{\text{ref}}$ . In this work, we pay attention to the measured frequencies ranging from 0.0026 Hz to 0.0547 Hz, with  $f_K = 0.0234$  Hz fixed, approximately corresponding to  $k_{\text{ref}} = 3.7 \times 10^{-7} \text{ m}^{-1}$ . We aim to explore the power spectral anisotropy of solar wind turbulence and its long-term (solar-cycle) variability through two independent tests: the ratio test and the anisotropy test, as defined in Equations (15) and (18), respectively. Specifically, we investigate the fraction of the slab component (as defined in Equation (16)) in the solar wind turbulence and its solar-cycle variations.

### 3. Data and Methods

We utilize the magnetic field and solar wind data of 3-second resolution collected by Wind spacecraft during the time period from January 1995 to December 2023, which covers nearly three solar cycles. The data of magnetic field and solar wind velocity were provided by Magnetic Field Investigation (Lepping et al. 1995) and Three-Dimensional Plasma and Energetic Particle Investigation (Lin et al. 1995) instruments on board Wind spacecraft, respectively. In this work, we do not aim to investigate the short-term features of solar wind turbulence during some specific events, such as solar energetic particle (SEP) events (Bieber et al. 1996) and corotating interaction regions (Tessein et al. 2011). Rather, we will investigate the more general properties of the power spectral anisotropy of solar wind turbulence in the context of solar activity and solar cycle.

A critical aspect of our analyses is to choose an appropriate time interval for determining the spectral properties of solar wind turbulence. The time interval needs to be long enough to provide reliable statistical estimates from sufficient observational data, and meanwhile short enough to maintain the temporal correlation required for effective correlation tensor calculations. Following the operation in Wanner & Wibberenz (1993), in the calculations we use 30-minute intervals, which are partly overlapping in our analyses. Furthermore, each time interval should satisfy such requirements: the missing data are less than 2%, and there are no consecutive missing data points. We further use the linear interpolation method to fill the small data gaps.

In the field-aligned coordinate system, we employ the pre-whitening and post-darkening procedures to improve our spectral analysis results (Bieber et al. 1993). The pre-whitening procedure is used to compute the first-order difference between successive magnetic field measurements for removing the mean field influence, and to isolate the fluctuating components for subsequent analyses. The autocorrelation function of the pre-whitened time series data is then computed up to a time lag of 192 seconds. We further use the discrete Fourier transform operation to obtain the power spectra of the first-order difference of the magnetic fields. The post-darkening corrections are then utilized to recover the original spectral slopes, by minimizing the distortions caused by the pre-whitening process.

We only retain the time intervals revealing a clear power-law feature within the inertial range for further analyses. We discard the power spectra containing negative spectral indices (i.e.,  $q < 0$ ), which are false values arising from the noises during the Blackman-Tukey analyses (Blackman & Tukey 1958). To avoid the influence of potential aliasing, we discard the upper two thirds of the frequencies in the power spectra. We pay attention to the remaining 21 frequency points from 0.0026 to 0.0547 Hz, corresponding to the timescales approximately from 18 to 384 seconds.

In our analyses, the millions of time intervals in each year of 1995-2023 can provide us with sufficient samples for statistically examining the 3D geometry of solar wind turbulence. We employ two independent methods, i.e., the so-called spectrum ratio test and spectrum anisotropy test, as described in Equations (15) and (18), respectively, to quantify the distribution of turbulence energy in different wavevector directions. For the spectrum ratio test, we calculate the ratio  $P_{\perp}/P_{\parallel}$  of the perpendicular to parallel power spectra. Generally, it is assumed that the slab fraction  $r$  is independent of the frequencies in the frequency range of interest (Bieber et al. 1996; Leamon et al. 1998). The ratio  $P_{\perp}/P_{\parallel}$  is computed at a fixed frequency of 0.0234 Hz, which is the midpoint of the considered frequency range. A ratio value close to unity implies that the turbulence mode with wavevectors parallel to the mean magnetic field is dominant, whereas the higher values suggest larger contributions from perpendicular wavevectors. We employ the anisotropy test to evaluate the dependence of the normalized total energy spectrum  $[f_K P_{\text{total}}(f_K)]_{\text{NORM}}$  on the field-to-flow angle  $\psi$ . Bieber et al. (1996) assumed that the normalized total energy  $E$  is independent of the angle  $\psi$ . However, the observational evidence presented in Saur & Bieber (1999) revealed that  $E$  roughly doubles when the angle  $\psi$  increases from  $0^\circ$  to  $90^\circ$ . Therefore, in this work we regard  $E$  as dependent on the angle  $\psi$ . For both tests, the field-to-flow angle  $\psi$  ranging from  $0^\circ$  to  $90^\circ$  is divided into nine bins with equal width ( $10^\circ$ ). Within each bin, we calculate the geometric means of the spectral ratios and normalize the total energy spectrum values to characterize the geometry of the solar wind turbulence.

## 4. Results and Discussion

### 4.1. Geometry of the Solar Wind Turbulence

We analyze the geometry of the solar wind turbulence during a time period of nearly three solar cycles (1995-2023). For each year, we calculate the geometric mean of the ratio

$P_{\perp}/P_{\parallel}$  of the perpendicular to parallel power spectral densities at the frequency of 0.0234 Hz. Table 1 shows the ratio values in each year, which range from 1.38 to 1.59, with an overall geometric mean of 1.51. Our results agree well with the ratio value  $\sim 1.40$  reported by Bieber et al. (1996), reinforcing the thought that the solar wind turbulence should be preferably described by the slab+2D two-component composite model. In the slab+2D composite model, the pure slab mode ( $r = 1$ ) corresponds to the ratio value ( $P_{\perp}/P_{\parallel}$ ) of unity, while the pure 2D mode ( $r = 0$ ) corresponds to the specific ratio value equal to the spectral index  $q$  ( $q = 5/3$ , if a Kolmogorov-like spectrum is assumed). These relations can be easily inferred in Equation (15). The values of ratio  $P_{\perp}/P_{\parallel}$  shown in Table 1 indicate that the 2D component is approximately dominant in the solar wind turbulence.

Figure 1 presents the results of the spectrum ratio test and spectrum anisotropy test using the data during the period 1995–2023. The left panel of Figure 1 shows the ratio  $P_{\perp}/P_{\parallel}$  as a function of the field-to-flow angle  $\psi$ . As we can see, the ratio initially increases with increasing  $\psi$  and peaks between  $60^{\circ}$  and  $70^{\circ}$ . The solid line denotes the fitting result of the slab+2D composite model, which determines the value of slab fraction, i.e.,  $r_{\text{ratio}} = 0.27$ . This indicates that approximately 73% of the turbulence energy is associated with the 2D component, and the remaining 27% of the energy is associated with the slab component. Therefore, the solar wind turbulence is 2D-component dominated, which agrees with the previous studies. The dashed line denotes the prediction of pure slab model (i.e.,  $r \equiv 1$ ), which systematically underestimates the observational values of the ratio  $P_{\perp}/P_{\parallel}$  for all the field-to-flow angles  $\psi$ . This discrepancy reveals the inadequacy of the pure slab model for describing the realistic geometry of the solar wind turbulence. Instead, the two-component composite model dominated by the 2D mode is much more appropriate for depicting the observations.

The right panel of Figure 1 presents the normalized total energy spectrum

$[f_K P_{\text{total}}(f_K)]_{\text{NORM}}$  as a function of the field-to-flow angle  $\psi$ . The normalized turbulence power increases by a factor of  $\sim 3$  as  $\psi$  varies from  $0^\circ$  to  $90^\circ$ . Fitting the composite model to the observations gives a slab fraction  $r_{\text{aniso}} = 0.13$ , which means that roughly 87% of the turbulence energy is associated with the 2D component. As in the left panel, the pure slab model ( $r = 1$ , dashed line) almost completely deviates from the observations. Therefore, the slab+2D composite model is more reasonable for interpreting the observations. As we can see, both the tests reveal the similar small slab fraction values, which indicates that the 2D component is dominant in the solar wind turbulence. Our results are in agreement with the previous studies (Bieber et al. 1996; Leamon et al. 1998).

## 4.2. Solar-cycle Variability of Composite Geometry

We analyze the long-term variation of the slab fraction during the 29-year time period to explore the solar-cycle variability of the composite geometry in the solar wind turbulence. In addition to ratio  $P_\perp/P_\parallel$ , Table 1 also presents other key quantities for each year during 1995-2023: mean field-to-flow angle  $\psi$ , slab fraction  $r_{\text{ratio}}$  derived from the spectrum ratio test, slab fraction  $r_{\text{aniso}}$  derived from the spectrum anisotropy test, and the averaged slab fraction  $\bar{r}$  of  $r_{\text{ratio}}$  and  $r_{\text{aniso}}$ . The slab fraction  $r_{\text{ratio}}$  ranges from 0.17 to 0.39, and  $r_{\text{aniso}}$  ranges from approximately 0.00 to 0.24. We can see that the slab fraction values from the spectrum ratio test are systematically larger than those from the spectrum anisotropy test. The most pronounced discrepancy occurs in 1996, where  $r_{\text{aniso}} = 0$  and  $r_{\text{ratio}} = 0.28$ . The overall value of  $r_{\text{ratio}}$  (0.27) is approximately twice that of  $r_{\text{aniso}}$  (0.13) for the time period 1995-2023. The averaged slab fraction  $\bar{r}$  of  $r_{\text{ratio}}$  and  $r_{\text{aniso}}$  suggests that approximately 71% – 87% of the total turbulence energy within the inertial range is distributed in the 2D component. That is to say, for quite a long time period (1995-2023), the 2D component almost always remains dominant in the energy anisotropy of the solar wind turbulence.

The left panel of Figure 2 shows the temporal evolutions of the slab fraction  $r_{\text{ratio}}$  derived from the spectrum ratio test and the sunspot number during the period 1995-2023. The slab fraction  $r_{\text{ratio}}$  generally fluctuates around 0.27, with a minimum of 0.17 in 2018. Interestingly, the larger slab fraction values tend to coincide with the increased sunspot numbers, and the smaller slab fraction values roughly accompany the decreased sunspot numbers. This phenomenon indicates that the solar activity influences the geometry of the solar wind turbulence. The right panel of Figure 2 shows the variations of slab fraction  $r_{\text{ratio}}$  with the increase of the sunspot number. The correlation coefficient between  $r_{\text{ratio}}$  and the sunspot number is 0.61. This finding means that the intense solar activity generally enhances the field-aligned turbulence. However, the 2D component always remains dominant, even during the periods of solar maxima. The empirical functional relation (black curve) between the slab fraction  $r_{\text{ratio}}$  and the sunspot number  $S_N$  can be described as

$$r_{\text{ratio}} = 0.19 \times S_N^{0.1}. \quad (19)$$

The left panel of Figure 3 presents the temporal evolutions of the slab fraction  $r_{\text{aniso}}$  derived from the spectrum anisotropy test and the sunspot number during 1995-2023. Generally, the slab fraction  $r_{\text{aniso}}$  fluctuates around 0.15, which suggests that roughly 85% of the turbulence energy in the inertial range is associated with the wavevectors perpendicular to the mean magnetic field. The right panel of Figure 3 displays the variations of slab fraction  $r_{\text{aniso}}$  with the increase of the sunspot number. The correlation coefficient between  $r_{\text{aniso}}$  and the sunspot number is 0.65. As mentioned above, the intense solar activity enhances the turbulence of the field-aligned component. Nevertheless, the essential manifestation is still that the 2D component remains dominant in the solar wind turbulence throughout the entire solar cycles. The empirical relation (black curve) between

the slab fraction  $r_{\text{aniso}}$  and the sunspot number  $S_N$  can be expressed as

$$r_{\text{aniso}} = 0.07 \times S_N^{0.2}. \quad (20)$$

The above consistent results from the two types of test methods show that the solar activity accompanying the solar cycles significantly influences the 3D geometry of solar wind turbulence in the inertial range. Specifically, the slab component in the solar wind turbulence is enhanced during the rise phases of the solar cycles. The increase of slab fraction is likely due to the intensified interplanetary magnetic field magnitude during the rise phases of the solar activity cycles. As we know, the Alfvén speed  $v_A$  is related to the interplanetary magnetic field magnitude  $B_0$  as

$$v_A = \frac{B_0}{\sqrt{\mu_0 \varrho_0}}, \quad (21)$$

where  $\mu_0$  is the permeability, and  $\varrho_0$  is the plasma density. Thus, the Alfvén speed  $v_A$  increases with the increasing magnetic field magnitude  $B_0$  during the rise phases of the solar cycles. Generally, the larger Alfvén speed indicates the larger slab fraction in the solar wind turbulence. Therefore, the slab fraction increases with the increasing sunspot number during the rise phases of the solar cycles.

## 5. Summary

In this work, we investigate the temporal evolutions of the 3D geometry of solar wind turbulence and particularly its solar-cycle variability during the time period 1995-2023. We use the so-called spectrum ratio test and spectrum anisotropy test to analyze the magnetic field and solar wind data of 3-second resolution collected by Wind spacecraft. The distribution of turbulence energy between the slab and 2D components in the inertial range is determined. Our results show that the solar wind turbulence is 2D-component



dominated, i.e.,  $\sim 80\%$  of the turbulence energy is in the 2D component. Our results agree well with the previous studies (Bieber et al. 1996; Leamon et al. 1998), which reinforces the viewpoint that most turbulence energy is associated with the wavevectors perpendicular to the mean magnetic field.

More significantly, both the ratio test and anisotropy test reveal that there exists a positive correlation between the slab fractions and the sunspot numbers accompanying the solar activity cycles. The correlation coefficients between the slab fractions and the sunspot numbers determined with the ratio test and anisotropy test are 0.61 and 0.65, respectively. That is to say, the slab fraction is enhanced during the rise phases (with increasing sunspot number) of the solar cycles. These findings show that the solar activity accompanying the solar cycles considerably influences the slab fraction (also 2D fraction) and the 3D composite geometry of the solar wind turbulence. The enhancement of slab fraction is associated with the intensified interplanetary magnetic field magnitude and consequently the increased Alfvén speed  $v_A$  during the rise phases of the solar cycles.

Our results presented in this work will be valuable for achieving an in-depth understanding of the 3D composite geometry and spectral anisotropy of the solar wind turbulence, and particularly of their solar-cycle variability. We suggest that the modulation effects of solar activity and solar cycles should be taken into account when we refine the solar wind turbulence models and especially the anisotropy models. The knowledge of solar wind turbulence and its anisotropy is crucial for the studies of several important topics in space physics and heliophysics, such as cosmic ray propagation and modulation, SEP acceleration and transport, and solar wind heating and acceleration, etc. Therefore, our findings will provide some new insights into these traditional subjects. In the future, we shall further investigate the solar wind turbulence anisotropy and its solar-cycle variations, so as to lay physical foundations for this interesting subject and the relevant topics.

This work was supported in part by the B-type Strategic Priority Program of the Chinese Academy of Sciences under grant XDB41000000, and the National Natural Science Foundation of China under grant 41874207. H.-Q. He gratefully acknowledges the partial support of the Youth Innovation Promotion Association of the Chinese Academy of Sciences (No. 2017091). We benefited from the data of Wind provided by NASA/Space Physics Data Facility (SPDF)/CDAWeb. The sunspot data were provided by the World Data Center SILSO, Royal Observatory of Belgium, Brussels.

## REFERENCES

- Bieber, J. W., Chen, J., Matthaeus, W. H., Smith, C. W., & Pomerantz, M. A. 1993, J. Geophys. Res., 98, 3585
- Bieber, J. W., Wanner, W., & Matthaeus, W. H. 1996, J. Geophys. Res., 101, 2511
- Blackman, R. B., & Tukey, J. W. 1958, Bell Syst. Tech. J., 37, 185
- Bruno, R., & Carbone, V. 2013, Living Rev. Sol. Phys., 10, 2
- Chen, C. H. K. 2016, Journal of Plasma Physics, 82, 535820602
- Dasso, S., Milano, L. J., Matthaeus, W. H., & Smith, C. W. 2005, ApJ, 635, L181
- Forman, M. A., Wicks, R. T., & Horbury, T. S. 2011, ApJ, 733, 76
- Goldreich, P., & Sridhar, S. 1995, ApJ, 438, 763
- Goldstein, M. L., Roberts, D. A., & Matthaeus, W. H. 1995, ARA&A, 33, 283
- He, H.-Q. 2015, ApJ, 814, 157
- He, H.-Q. 2021, Monthly Notices of the Royal Astronomical Society: Letters, 508, L1
- Horbury, T. S., Forman, M., & Oughton, S. 2008, Phys. Rev. Lett., 101, 175005
- Jokipii, J. R., & Hollweg, J. V. 1970, ApJ, 160, 745
- Leamon, R. J., Smith, C. W., Ness, N. F., Matthaeus, W. H., & Wong, H. K. 1998, J. Geophys. Res., 103, 4775
- Lepping, R. P., Acuña, M. H., Burlaga, L. F., et al. 1995, Space Sci. Rev., 71, 207
- Lin, R. P., Anderson, K. A., Ashford, S., et al. 1995, Space Sci. Rev., 71, 125

- Matthaeus, W. H., Goldstein, M. L., & Roberts, D. A. 1990, *J. Geophys. Res.*, 95, 20673
- Matthaeus, W. H., Gray, P. C., Pontius, Jr., D. H., & Bieber, J. W. 1995, *Phys. Rev. Lett.*, 75, 2136
- Matthaeus, W. H., & Smith, C. 1981, *Phys. Rev. A*, 24, 2135
- Narita, Y. 2018, *Living Rev. Sol. Phys.*, 15, 1
- Nieuwstadt, F. T. M., Westerweel, J., & Boersma, B. J. 2016, *Turbulence: Introduction to Theory and Applications of Turbulent Flows* (Cham, Switzerland: Springer)
- Osman, K. T., & Horbury, T. S. 2007, *ApJ*, 654, L103
- Oughton, S., & Engelbrecht, N. E. 2021, *New A*, 83, 101507
- Oughton, S., Matthaeus, W. H., Wan, M., & Osman, K. T. 2015, *Philosophical Transactions of the Royal Society A: Mathematical, Physical and Engineering Sciences*, 373, 20140152
- Oughton, S., Priest, E. R., & Matthaeus, W. H. 1994, *Journal of Fluid Mechanics*, 280, 95
- Parker, E. N. 1979, *Cosmical Magnetic Fields: Their Origin and Their Activity* (Oxford: Oxford Univ. Press)
- Saur, J., & Bieber, J. W. 1999, *J. Geophys. Res.*, 104, 9975
- Shebalin, J. V., Matthaeus, W. H., & Montgomery, D. 1983, *Journal of Plasma Physics*, 29, 525
- Taylor, G. I. 1938, *Proceedings of the Royal Society of London Series A: Mathematical and Physical Sciences*, 164, 476

- Tessein, J. A., Smith, C. W., Vasquez, B. J., & Skoug, R. M. 2011, *J. Geophys. Res.*, 116, A10103
- Tu, C.-Y., & Marsch, E. 1995, *Space Sci. Rev.*, 73, 1
- Velli, M. 2003, *Plasma Physics and Controlled Fusion*, 45, A205
- Wanner, W., & Wibberenz, G. 1993, *J. Geophys. Res.*, 98, 3513
- Wicks, R. T., Horbury, T. S., Chen, C. H. K., & Schekochihin, A. A. 2010, *Monthly Notices of the Royal Astronomical Society: Letters*, 407, L31
- Zank, G. P., & Matthaeus, W. H. 1992, *Journal of Plasma Physics*, 48, 85
- Zank, G. P., Nakanotani, M., Zhao, L.-L., Adhikari, L., & Telloni, D. 2020, *ApJ*, 900, 115
- Zhou, G., & He, H.-Q. 2021, *ApJ*, 911, L2
- Zhou, G., He, H.-Q., & Wan, W. 2020, *ApJ*, 899, L32
- Zhou, Y., & Matthaeus, W. H. 1990, *J. Geophys. Res.*, 95, 14881

Table 1: The computation results of the key quantities during the time period 1995-2023: mean field-to-flow angle  $\psi$ , geometric mean of  $P_{\perp}/P_{\parallel}$ , slab fraction  $r_{\text{ratio}}$  derived from the spectrum ratio test, slab fraction  $r_{\text{aniso}}$  derived from the spectrum anisotropy test, and the averaged slab fraction  $\bar{r}$  of  $r_{\text{ratio}}$  and  $r_{\text{aniso}}$ .

Year	$\psi$ ( $^{\circ}$ )	$P_{\perp}/P_{\parallel}$	$r_{\text{ratio}}$	$r_{\text{aniso}}$	$\bar{r}$
1995-2023	52.86	1.51	0.27	0.13	0.20
1995	51.75	1.49	0.27	0.13	0.20
1996	48.66	1.43	0.28	0.00	0.14
1997	53.20	1.50	0.27	0.17	0.22
1998	54.17	1.53	0.22	0.18	0.20
1999	53.08	1.41	0.39	0.19	0.29
2000	54.03	1.48	0.32	0.20	0.26
2001	54.63	1.47	0.31	0.16	0.24
2002	53.89	1.49	0.31	0.24	0.27
2003	48.77	1.38	0.36	0.15	0.26
2004	49.77	1.42	0.34	0.15	0.24
2005	51.68	1.52	0.24	0.13	0.18
2006	53.71	1.51	0.28	0.11	0.20
2007	51.41	1.50	0.23	0.08	0.15
2008	52.10	1.50	0.25	0.16	0.21
2009	54.91	1.58	0.23	0.12	0.17
2010	53.99	1.55	0.26	0.14	0.20
2011	53.48	1.52	0.24	0.18	0.21
2012	56.91	1.59	0.29	0.09	0.19
2013	55.25	1.59	0.27	0.16	0.22
2014	55.65	1.59	0.23	0.17	0.20
2015	52.66	1.55	0.22	0.12	0.17
2016	52.18	1.49	0.28	0.17	0.22
2017	50.26	1.48	0.24	0.10	0.17
2018	51.11	1.51	0.17	0.09	0.13
2019	51.83	1.50	0.21	0.09	0.15
2020	52.10	1.51	0.23	0.13	0.18
2021	54.46	1.55	0.25	0.11	0.18
2022	54.11	1.53	0.28	0.21	0.24
2023	55.35	1.54	0.33	0.14	0.23

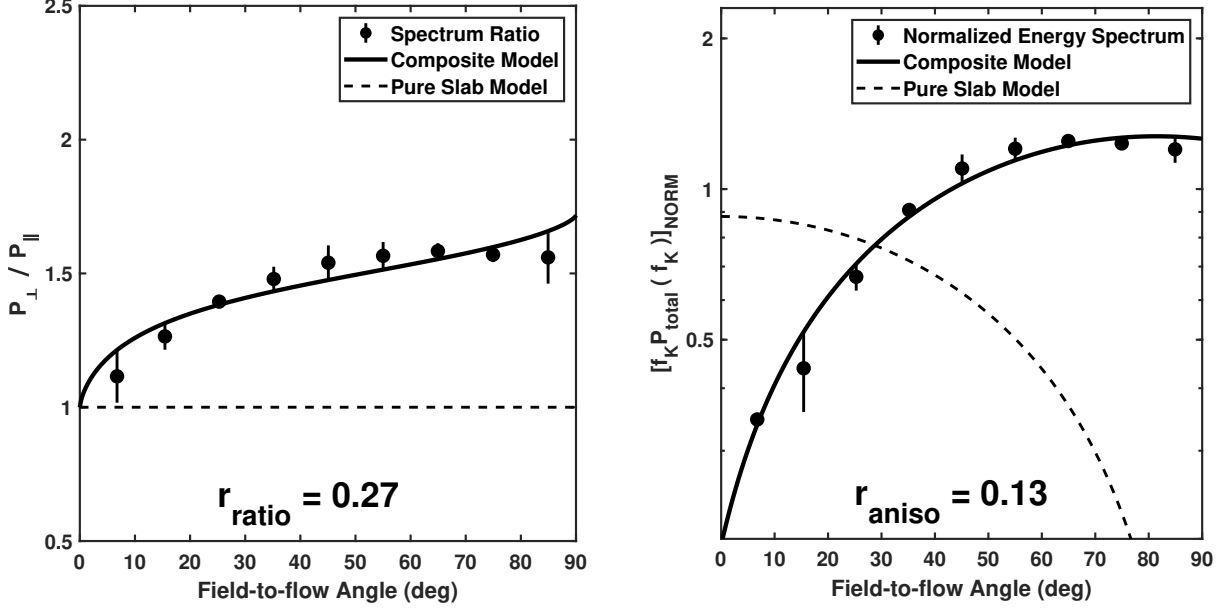


Fig. 1.— Left: ratio  $P_{\perp}/P_{\parallel}$  of perpendicular to parallel power spectra as a function of field-to-flow angle  $\psi$ . The composite model (solid line) consisting of 73% 2D and 27% slab turbulence is consistent with the observations (data points). The dashed line denotes the pure slab model ( $r = 1$ ), which significantly deviates from the observations. Right: normalized total energy spectrum  $[f_K P_{\text{total}}(f_K)]_{\text{NORM}}$  as a function of field-to-flow angle  $\psi$ . The composite model (solid line) consisting of 87% 2D and 13% slab turbulence is consistent with the observations (data points). Again, the pure slab model ( $r = 1$ , dashed line) significantly deviates from the realistic observations.

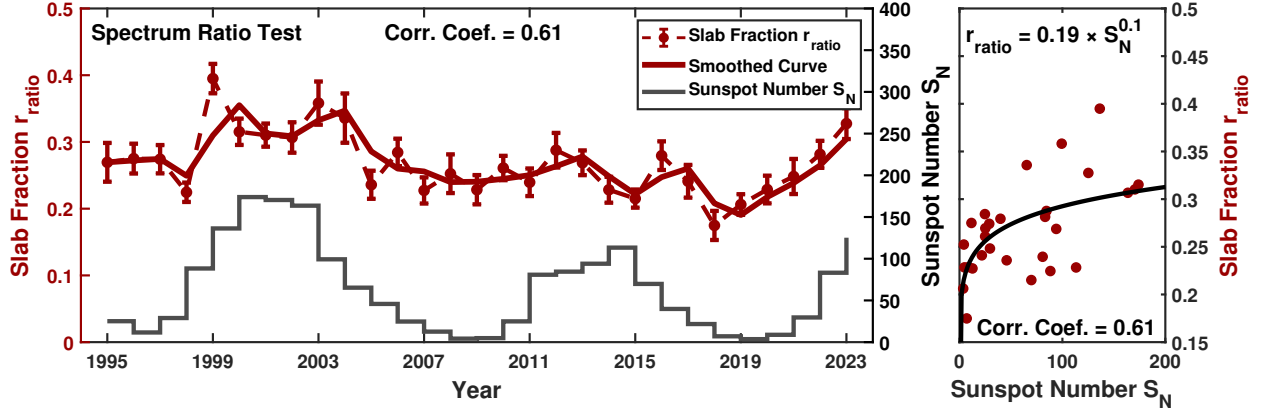


Fig. 2.— Left: temporal evolutions of the sunspot number  $S_N$  (grey line) and the slab fraction  $r_{\text{ratio}}$  (red circles) derived from the spectrum ratio test during the time period 1995-2023. The red solid line denotes the smoothed results of  $r_{\text{ratio}}$ . Right: variations of the slab fraction  $r_{\text{ratio}}$  with the increase of the sunspot number. The correlation coefficient between  $r_{\text{ratio}}$  and the sunspot number is 0.61.



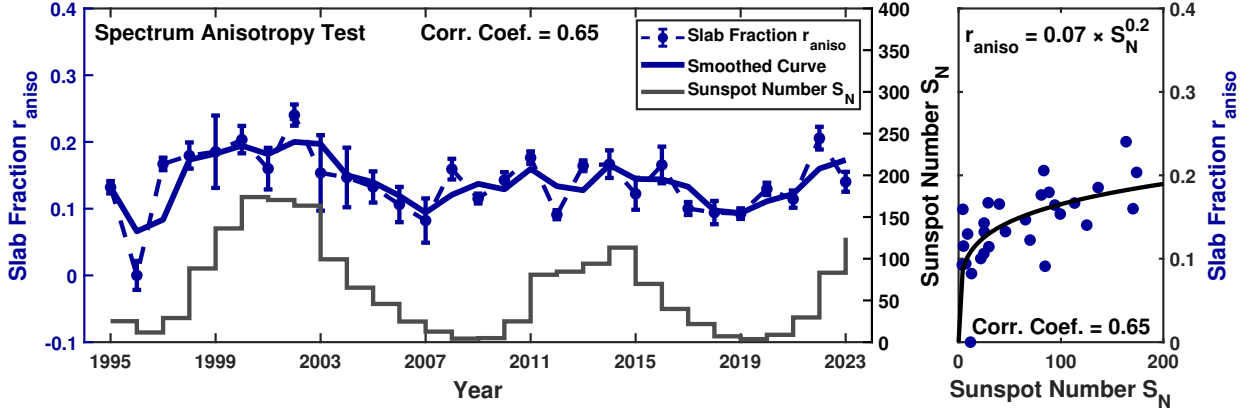


Fig. 3.— Left: evolutions of the sunspot number  $S_N$  (grey line) and the slab fraction  $r_{\text{aniso}}$  (blue circles) derived from the spectrum anisotropy test during the period 1995-2023. The blue solid line denotes the smoothed results of  $r_{\text{aniso}}$ . Right: variations of the slab fraction  $r_{\text{aniso}}$  with the increase of the sunspot number. The correlation coefficient between  $r_{\text{aniso}}$  and the sunspot number is 0.65.